The Astrophysical Journal, 700:762–773, 2009 July 20 doi:10.1088/0004-637X/700/1/762

THE TEMPERATURE AND DENSITY STRUCTURE OF THE SOLAR CORONA. I. OBSERVATIONS OF THE QUIET SUN WITH THE EUV IMAGING SPECTROMETER ON *HINODE*

Harry P. Warren and David H. Brooks[1]
Space Science Division, Naval Research Laboratory, Washington, DC 20375, USA
Received 2009 January 12; accepted 2009 May 7; published 2009 July 6

ABSTRACT

Measurements of the temperature and density structure of the solar corona provide critical constraints on theories of coronal heating. Unfortunately, the complexity of the solar atmosphere, observational uncertainties, and the limitations of current atomic calculations, particularly those for Fe, all conspire to make this task very difficult. A critical assessment of plasma diagnostics in the corona is essential to making progress on the coronal heating problem. In this paper, we present an analysis of temperature and density measurements above the limb in the quiet corona using new observations from the EUV Imaging Spectrometer (EIS) on *Hinode*. By comparing the Si and Fe emission observed with EIS we are able to identify emission lines that yield consistent emission measure distributions. With these data we find that the distribution of temperatures in the quiet corona above the limb is strongly peaked near 1 MK, consistent with previous studies. We also find, however, that there is a tail in the emission measure distribution that extends to higher temperatures. EIS density measurements from several density sensitive line ratios are found to be generally consistent with each other and with previous measurements in the quiet corona. Our analysis, however, also indicates that a significant fraction of the weaker emission lines observed in the EIS wavelength ranges cannot be understood with current atomic data.

Key words: Sun: corona

Online-only material: color figures

1. INTRODUCTION

The origin of the high-temperature plasma that permeates the solar corona has defied understanding for many decades. In principal, the thermal structure of the solar corona holds many clues to the physical processes that convert magnetic energy into thermal energy. For example, it has been proposed that the corona is heated by frequent bursts of magnetic reconnection called nanoflares (e.g., Parker 1972, 1983). In this model, turbulent motions in the solar photosphere lead to the constant tangling and braiding of the magnetic fields that rise up into the corona. The dissipation of this topological complexity leads to the release of energy on very small spatial scales. This suggests that the corona should be composed of many fine loops that are in various stages of heating and cooling. Thus, the distribution of temperatures and densities is a critical constraint on the frequency, duration, and magnitude of the heating events that give rise to the high-temperature corona.

Unfortunately, determining the distribution of temperatures and densities in the corona is a nontrivial problem. The solar corona is highly structured and highly dynamic, making it difficult to isolate individual structures. Obtaining accurate atomic calculations is also a problem. Because of its relatively high elemental abundance, emission from Fe has been the focus of many recent solar instruments. Interpreting observations from imaging instruments such as the Soft X-ray Telescope (SXT)/*Yohkoh*, the EUV Imaging Telescope (EIT)/*SOHO*, the *Transition Region and Coronal Explorer* (*TRACE*), the EUVI/*STEREO*, the XRT/*Hinode*, and the upcoming AIA/*SDO* depends critically on accurate atomic calculations for Fe. The accuracy of the available atomic calculations for this complex atom, however, is often unclear.

The launch of the EUV Imaging Spectrometer (EIS) on *Hinode* has greatly expanded spectroscopic observations of the solar corona. EIS combines a broad temperature coverage (Fe VIII–Fe XVII, Fe XXII–Fe XXIV) with relatively high spatial (1″) and spectral (22 mÅ) resolution, allowing the temperature and density structure of the corona to be examined in great detail. Of particular interest are the properties of coronal loops observed in solar active regions and flares. Current models of active region loops suggest that the observed densities and temperatures are signatures of nonequilibrium processes, and EIS, with its advanced diagnostic capabilities, provides much stricter observational constraints on physical models. Recent work on the properties of active region loops, for example, has suggested that active region loops near 1 MK have narrow distributions of temperature, high densities, and relatively small filling factors (Warren et al. 2008).

Since many of the plasma diagnostics provided by EIS are based on Fe emission lines it is important to assess them critically and compare results with previous measurements. Some initial results have been alarming. For example, EIS spectroheliograms in Fe VIII and Si VII are nearly identical, suggesting a very similar temperature of formation (Young et al. 2007). The respective peaks in the ionization fractions, however, are separated by over 0.2 MK. This calls into question how accurately temperatures can be measured using the Fe emission observed in the EIS wavelength ranges.

In this paper, we present an analysis of EIS observations above the quiet solar limb. Many previous observations of the quiet corona have suggested that the distribution of temperatures is very narrow, almost isothermal (e.g., Raymond et al. 1997; Feldman et al. 1998; Feldman et al. 1999a; Warren 1999; Allen et al. 2000; Landi et al. 2002; Warren & Warshall 2002). By comparing Fe and Si emission observed with EIS we are able to identify plasma diagnostics that are both self-consistent and in agreement with earlier results. Fortunately, most of the useful

[1] Also at the College of Science, George Mason University, 4400 University Drive, Fairfax, VA 22030, USA.

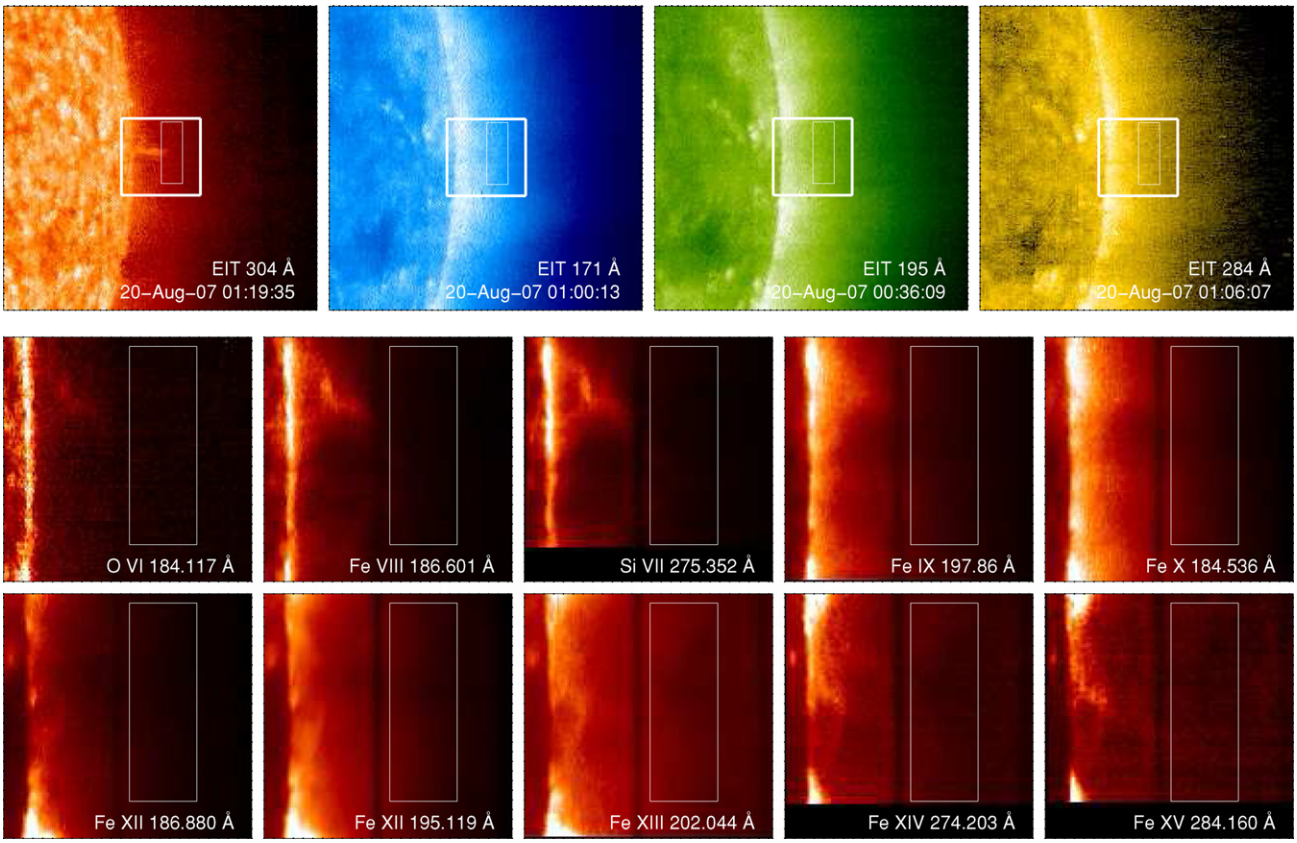

Figure 1. Top panels: EIT images taken during the EIS full CCD observations. The boxes indicate the EIS field of view and the region used for computing the average spectra. Bottom panels: EIS spectroheliograms in selected emission lines. The dark vertical band in each image is due to atmospheric absorption during a brief orbital eclipse.

(A color version of this figure is available in the online journal.)

diagnostics that are identified are the strongest emission lines that can be observed with EIS. However, our analysis also shows that a significant fraction of the observed emission lines cannot be understood with current atomic models.

In this work, we also apply a Monte Carlo Markov Chain (MCMC) emission measure algorithm (Kashyap & Drake 1998, 2000) to the observed EIS spectra and find that the distribution of temperatures in the quiet corona is more complicated than previously thought. The emission measure is sharply peaked near 1 MK, as was found in earlier studies. We also find, however, a tail in the emission measure distribution that extends to higher temperatures. A high-temperature component to the emission measure distribution is a critical element of impulsive coronal heating models (e.g., Cargill & Klimchuk 2004; Patsourakos & Klimchuk 2008).

Previous measurements of electron densities in the quiet corona above the limb have yielded values of $\log n_e \sim 8.3$ (e.g., Doschek et al. 1997). EIS has several density sensitive line ratios that are useful in the quiet corona. We find that these ratios are all generally consistent with each other and with previous results, although there is considerable dispersion in the densities inferred from EIS.

Finally, we also discuss the potential for measuring relative abundances in the corona using the S X 264.233 Å and O VI 184.117 Å lines observed with EIS.

2. INSTRUMENTATION AND DATA REDUCTION

The EIS instrument on *Hinode* produces stigmatic spectra in two wavelength ranges (171–212 Å and 245–291 Å) with a spectral resolution of 0.0223 Å (Culhane et al. 2007; Korendyke et al. 2006). There are 1″ and 2″ slits as well as 40″ and 266″ slots available. The slit-slot mechanism is 1024″ long but a maximum of 512 pixels on the CCD can be read out at one time. Solar images can be made using one of the slots or by stepping one of the slits over a region of the Sun. Telemetry constraints generally limit the spatial and spectral coverage of an observation. For this work we focus on the results from a special observing sequence (`HPW_FULLCCD_001`) that returned the entire wavelength range of the CCD over a small region on the Sun (128″ × 128″). At each position in the raster a 90 s exposure is taken.

The data for this study were taken between 2007 August 19 23:47 UT and 2007 August 20 03:01 at the west limb. Context images from the EUV Imaging Telescope on *SOHO* (Delaboudinière et al. 1995) are shown in Figure 1 and indicate that the observed region was quiet during this time. The inspection of EIT 195 Å movies during this period shows no indication of significant coronal activity. The EIT 304 Å image does indicate the presence of some cool material at low heights in the corona.

These EIS data were processed using standard algorithms to remove the CCD pedestal, dark current, "cosmic ray" spikes, and warm pixels. The data numbers recorded in each pixel were also converted to physical units (erg cm^{-2} s^{-1} sr^{-1} $\mathrm{Å}^{-1}$). For each intensity value an uncertainty is also calculated. This uncertainty includes counting statistics and read noise, but not the uncertainty associated with the absolute calibration. The implications of this will be discussed in later sections.

There are several instrumental effects that impact our analysis. The first is the oscillation in the line centroids. This

oscillation, which is about 2 spectral pixels in magnitude (~ 0.04 Å) over a period of about 90 minutes, is believed to be due to changing thermal conditions on the spacecraft during an orbit. To correct for this we assume that the average Doppler shift in the Fe XII 195.119 Å line averaged along the slit is zero at each slit position. Another important effect is the spatial offset between the two detectors. Because of a misalignment between the two CCDs there is a vertical offset of approximately 18 pixels between images taken in the different channels. In data taken before 2008 August 24 there is also an offset of 1–2 pixels in the solar-*X* direction.

After these instrumental effects are accounted for we can determine the line intensity at each spatial position by calculating either moment of the line profile or a Gaussian fit. For making context rasters we use moments and EIS rasters in selected lines are shown in Figure 1. These rasters also indicate the presence of some cool material at low heights in the corona.

Since our objective is to analyze observations from the quiet corona with very high signal to noise we have computed a spectrum averaged over a $35'' \times 104''$ region that lies above this cool material. The center of this region is about $70''$ above the limb or about 1.07 $R_\odot$. In constructing this average spectrum we have ignored any pixel that has been marked as a warm pixel or as a cosmic ray impact. The intensity in each spectral pixel is computed from the average of approximately 3400 spatial pixels.

We have used the identifications of Brown et al. (2008) and Young et al. (2007) to determine the emission lines of interest. For each of these lines we have fit the line profiles with Gaussians and extracted the relevant line intensities. These line intensities are given in Tables 1 and 2. Additionally, we extracted line intensities for three Fe IX lines that were recently identified by Young (2009). This list is not complete. The objective here is to consider the strongest emission lines that could be used in spatially resolved observations, and not to consider every emission line in the spectrum.

All of the lines except Fe XVI 262.984 Å are well represented by Gaussians. There is very little signal in the Fe XVI profile and the observed emission is essentially noise. This measurement does provide a very useful upper bound on the amount of high temperature emission in this region.

Tables 1 and 2 give the most significant atomic transitions for each emission line. The CHIANTI level numbers are also given in these tables. The level numbers are simply an ordered list of the transitions. They aid in identifying which emission lines involve transitions to the ground state as well as which lines originate in the same upper level. The Fe X 190.038 and 184.536 Å lines, for example, originate in the same upper level and form a branching ratio. The branching ratio only depends on the relative decay rates and should be more accurate than other ratios. In these tables the emissivity at the peak of the ionization fraction and a density of $\log n_e = 8.35$ is also given.

In addition to the Fe lines EIS also observes several weaker Si VII, IX, and X emission lines. Si emission lines from these ionization stages have been used in previous emission measure analysis of the quiet corona (e.g., Feldman et al. 1999a; Warren 1999; Landi et al. 2002; Warren & Warshall 2002) and provide a useful comparison for the analysis of the Fe lines.

Elemental abundances play an important role in determining the magnitude of radiative losses in the corona. There are several emission lines from high first ionization potential (FIP) elements observed within the EIS wavelength ranges (Feldman et al. 2009). At coronal temperatures the S X 264.233 Å and S XIII 256.686 Å lines can be used for studying the composition. Only the S X line appears in these data. The O VI lines at 183.937 and 184.117 Å provide another measurement from a high FIP element. O VI is Li-like and the ionization fraction for this ion is significant at coronal temperatures.

3. TEMPERATURE AND DENSITY MEASUREMENTS

The observed intensities are related to the plasma emissivities, $\epsilon_\lambda(n, T)$, and the differential emission measure, $\xi(T)$, by the expression

$$I_\lambda = \frac{1}{4\pi} \int \epsilon_\lambda(n_e, T) \xi(T)\, dT. \quad (1)$$

In this context, the plasma emissivities are the radiated power (erg s^{-1}) divided by the square of the electron number density, n_e. For many atomic transitions this quantity depends mainly on the electron temperature, T. For many of the Fe lines considered here, however, the emissivity is strongly dependent on the density, even for transitions to the ground state, and to facilitate intensity calculations we have computed grids of emissivities over a wide range of densities and temperatures using the CHIANTI 5.2.1 atomic physics database (e.g., Landi et al. 2006). The 5.2.1 version of the database corrects an error in the atomic data for Fe XIII. The abundances of Feldman et al. (1992) and the low-density ionization fractions of Mazzotta et al. (1998) are assumed. In this expression, the emission measure is the line-of-sight emission measure, $\xi(T) = n_e^2\, ds/dT$, and has units of cm^{-5} K^{-1}. In the plots, we will generally display the differential emission measure times the temperature.

For this work we will consider three different methods for reconstructing the differential emission measure from the EIS intensity measurements. The first two methods rely on a parameterization of the emission measure. The simplest approximation is that of a single temperature plasma where the differential emission measure is a delta function

$$\xi(T) = \mathrm{EM}_0\, \delta(T - T_0). \quad (2)$$

To account for the possibility that there is some dispersion in the temperature distribution we also consider a Gaussian representation of the differential emission measure

$$\xi(T) = \frac{\mathrm{EM}_0}{\sigma_T \sqrt{2\pi}} \exp\left[-\frac{(T - T_0)^2}{2\sigma_T^2}\right]. \quad (3)$$

The Gaussian DEM is parameterized so that for very narrow temperature distributions we recover the parameters for the isothermal case, i.e., for $T_0/\sigma_T \gg 1$ we have $\int \xi(T)\, dT \sim \mathrm{EM}_0$. To determine the best-fit parameters for either of these emission measure models we use a Levenberg–Marquardt technique implemented in the `MPFIT` package. We have implemented this algorithm so that the density in Equation (1) can either be a free parameter or have a fixed value.

Finally, we also apply a MCMC emission measure algorithm (Kashyap & Drake 1998, 2000) distributed with the `PINTofALE` spectral analysis package to these data. This algorithm has the advantage of not assuming a shape for the differential emission measure. The MCMC algorithm also provides for estimates of the error in the DEM. In its current implementation the MCMC algorithm does not allow for the density to be a free parameter.

Perhaps the most important test of the EIS spectra is the application of the isothermal DEM model to the observed Si emission. The atomic data for Si appears to be very well

Table 1
Fe Intensities Measured in the Quiet Corona above the Limb with EIS[a]

Ion	λ	T_{max}	Transition	L1	L2	ϵ_λ	I_{obs}	σ_{Iobs}	
Fe VIII	185.213	5.57	$3p^6\ 3d\ ^2D_{5/2}–3p^5\ 3d^2\ (^3F)\ ^2F_{7/2}$	2	46	6.23e-24	18.54 ±	0.11	
Fe VIII	186.601	5.57	$3p^6\ 3d\ ^2D_{3/2}–3p^5\ 3d^2\ (^3F)\ ^2F_{5/2}$	1	45	4.63e-24	14.60 ±	0.09	
Fe VIII	194.663	5.57	$3p^6\ 3d\ ^2D_{5/2}–3p^6\ 4p\ ^2P_{3/2}$	2	43	1.22e-24	5.38 ±	0.03	
Fe IX	171.073	5.81	$3s^2\ 3p^6\ ^1S_0–3s^2\ 3p^5\ 3d\ ^1P_1$	1	13	6.96e-23	921.27 ±	17.93	
Fe IX	188.497	5.81	$3s^2\ 3p^5\ 3d\ ^3F_4–3s^2\ 3p^4\ (^3P)\ 3d^2\ ^3G_5$	5	95	2.66e-24	31.28 ±	0.12	♡
Fe IX	189.941	5.81	$3s^2\ 3p^5\ 3d\ ^3F_3–3s^2\ 3p^4\ (^3P)\ 3d^2\ ^3G_4$	6	94	1.55e-24	15.36 ±	0.05	♡
Fe IX	197.862	5.81	$3s^2\ 3p^5\ 3d\ ^1P_1–3s^2\ 3p^5\ 4p\ ^1S_0$	13	140	1.65e-24	21.02 ±	0.06	♡
Fe X	174.532	5.99	$3s^2\ 3p^5\ ^2P_{3/2}–3s^2\ 3p^4\ (^3P)\ 3d\ ^2D_{5/2}$	1	30	2.64e-23	572.57 ±	4.44	♡
Fe X	177.239	5.99	$3s^2\ 3p^5\ ^2P_{3/2}–3s^2\ 3p^4\ (^3P)\ 3d\ ^2P_{3/2}$	1	28	1.44e-23	308.28 ±	1.75	♡
Fe X	184.536	5.99	$3s^2\ 3p^5\ ^2P_{3/2}–3s^2\ 3p^4\ (^1D)\ 3d\ ^2S_{1/2}$	1	27	5.68e-24	142.17 ±	0.29	♡
Fe X	190.038	5.99	$3s^2\ 3p^5\ ^2P_{1/2}–3s^2\ 3p^4\ (^1D)\ 3d\ ^2S_{1/2}$	2	27	1.60e-24	52.74 ±	0.11	
Fe X	207.449	5.99	$3s^2\ 3p^5\ ^2P_{3/2}–3s^2\ 3p^4\ (^1D)\ 3d\ ^2F_{5/2}$	1	23	3.49e-25	24.09 ±	0.25	
Fe X	257.262	5.99	$3s^2\ 3p^5\ ^2P_{3/2}–3s^2\ 3p^4\ (^3P)\ 3d\ ^4D_{7/2}$	1	5	2.57e-24	122.67 ±	0.25	
			$3s^2\ 3p^5\ ^2P_{3/2}–3s^2\ 3p^4\ (^3P)\ 3d\ ^4D_{5/2}$	1	4	6.51e-25			
Fe XI	180.401	6.07	$3s^2\ 3p^4\ ^3P_2–3s^2\ 3p^3\ (^4S)\ 3d\ ^3D_3$	1	42	1.75e-23	432.24 ±	1.00	♡
Fe XI	182.167	6.07	$3s^2\ 3p^4\ ^3P_1–3s^2\ 3p^3\ (^4S)\ 3d\ ^3D_2$	2	43	2.29e-24	58.50 ±	0.28	♡
Fe XI	188.216	6.07	$3s^2\ 3p^4\ ^3P_2–3s^2\ 3p^3\ (^2D)\ 3d\ ^3P_2$	1	38	8.20e-24	224.90 ±	0.25	♡
Fe XI	188.299	6.07	$3s^2\ 3p^4\ ^3P_2–3s^2\ 3p^3\ (^2D)\ 3d\ ^1P_1$	1	39	2.98e-24	153.09 ±	0.18	
Fe XI	192.813	6.07	$3s^2\ 3p^4\ ^3P_1–3s^2\ 3p^3\ (^2D)\ 3d\ ^3P_2$	2	38	1.71e-24	57.73 ±	0.12	♡
			$3s^2\ 3p^4\ ^3P_1–3s^2\ 3p^3\ (^2D)\ 3d\ ^3S_1$	2	37	3.86e-25			
Fe XI	257.547	6.07	$3s^2\ 3p^4\ ^3P_2–3s^2\ 3p^3\ (^4S)\ 3d\ ^5D_3$	1	13	2.33e-25	24.29 ±	0.13	
Fe XI	257.772	6.07	$3s^2\ 3p^4\ ^3P_2–3s^2\ 3p^3\ (^4S)\ 3d\ ^5D_2$	1	12	1.14e-25	11.72 ±	0.07	
Fe XII	186.880	6.13	$3s^2\ 3p^3\ ^2D_{5/2}–3s^2\ 3p^2\ (^3P)\ 3d\ ^2F_{7/2}$	3	39	1.90e-24	35.17 ±	0.13	♡
			$3s^2\ 3p^3\ ^2D_{3/2}–3s^2\ 3p^2\ (^3P)\ 3d\ ^2F_{5/2}$	2	36	3.40e-25			
Fe XII	192.394	6.13	$3s^2\ 3p^3\ ^4S_{3/2}–3s^2\ 3p^2\ (^3P)\ 3d\ ^4P_{1/2}$	1	30	5.67e-24	79.48 ±	0.12	♡
Fe XII	193.509	6.13	$3s^2\ 3p^3\ ^4S_{3/2}–3s^2\ 3p^2\ (^3P)\ 3d\ ^4P_{3/2}$	1	29	1.19e-23	177.53 ±	0.16	♡
Fe XII	195.119	6.13	$3s^2\ 3p^3\ ^4S_{3/2}–3s^2\ 3p^2\ (^3P)\ 3d\ ^4P_{5/2}$	1	27	1.77e-23	274.67 ±	0.17	♡
Fe XII	196.640	6.13	$3s^2\ 3p^3\ ^2D_{5/2}–3s^2\ 3p^2\ (^1D)\ 3d\ ^2D_{5/2}$	3	34	6.04e-25	11.03 ±	0.04	♡
Fe XII	203.720	6.13	$3s^2\ 3p^3\ ^2D_{5/2}–3s^2\ 3p^2\ (^1S)\ 3d\ ^2D_{5/2}$	3	32	7.35e-25	20.32 ±	0.12	
Fe XII	256.925	6.13	$3s^2\ 3p^3\ ^2D_{3/2}–3s^2\ 3p^2\ (^3P)\ 3d\ ^4F_{5/2}$	2	15	6.77e-26	39.09 ±	0.15	
			$3s\ 3p^4\ ^4P_{5/2}–3s3p^3\ 3d\ ^4D_{7/2}$	6	50	1.08e-26			
Fe XIII	196.525	6.19	$3s^2\ 3p^2\ ^1D_2–3s^2\ 3p\ 3d\ ^1F_3$	4	26	2.48e-25	2.71 ±	0.02	♡
Fe XIII	197.434	6.19	$3s^2\ 3p^2\ ^3P_0–3s^2\ 3p\ 3d\ ^3D_1$	1	23	7.54e-25	7.10 ±	0.04	♡
Fe XIII	200.021	6.19	$3s^2\ 3p^2\ ^3P_1–3s^2\ 3p\ 3d\ ^3D_2$	2	25	9.70e-25	9.43 ±	0.06	♡
Fe XIII	201.121	6.19	$3s^2\ 3p^2\ ^3P_1–3s^2\ 3p\ 3d\ ^3D_1$	2	23	3.68e-24	45.14 ±	0.12	
Fe XIII	202.044	6.19	$3s^2\ 3p^2\ ^3P_0–3s^2\ 3p\ 3d\ ^3P_1$	1	20	1.82e-23	157.66 ±	0.26	♡
Fe XIII	203.826	6.19	$3s^2\ 3p^2\ ^3P_2–3s^2\ 3p\ 3d\ ^3D_3$	3	24	2.86e-24	25.02 ±	0.16	♡
			$3s^2\ 3p^2\ ^3P_2–3s^2\ 3p\ 3d\ ^3D_2$	3	25	1.35e-24			
Fe XIII	204.937	6.19	$3s^2\ 3p^2\ ^3P_2–3s^2\ 3p\ 3d\ ^3D_1$	3	23	1.13e-24	8.19 ±	0.17	
Fe XIII	246.208	6.19	$3s^2\ 3p^2\ ^3P_1–3s\ 3p^3\ ^3S_1$	2	14	2.35e-24	9.36 ±	0.18	
Fe XIII	251.953	6.19	$3s^2\ 3p^2\ ^3P_2–3s\ 3p^3\ ^3S_1$	3	14	4.52e-24	19.33 ±	0.24	
Fe XIV	211.316	6.27	$3s^2\ 3p\ ^2P_{1/2}–3s^2\ 3d\ ^2D_{3/2}$	1	11	1.00e-23	39.47 ±	0.51	♡
Fe XIV	264.787	6.27	$3s^2\ 3p\ ^2P_{3/2}–3s\ 3p^2\ ^2P_{3/2}$	2	10	3.72e-24	20.72 ±	0.08	
Fe XIV	270.519	6.27	$3s^2\ 3p\ ^2P_{3/2}–3s\ 3p^2\ ^2P_{1/2}$	2	9	2.56e-24	6.96 ±	0.06	♡
Fe XIV	274.203	6.27	$3s^2\ 3p\ ^2P_{1/2}–3s\ 3p^2\ ^2S_{1/2}$	1	8	5.54e-24	18.31 ±	0.08	♡
Fe XV	284.160	6.33	$3s^2\ ^1S_0–3s\ 3p\ ^1P_1$	1	5	2.88e-23	21.20 ±	0.14	?
Fe XVI	262.984	6.43	$3p\ ^2P_{3/2}–3d\ ^2D_{5/2}$	3	5	9.18e-25	0.42 ±	0.04	?

Notes.
[a] In this and all subsequent tables wavelengths are in Å and the units for the intensities and the corresponding uncertainties are erg cm^{-2} s^{-1} sr^{-1}. Lines that can be used for emission measure analysis are indicated by the "♡" symbol. There is no independent check on the Fe XV 284.160 Å and Fe XVI 262.984 Å lines so they are marked with a "?".

understood and previous emission measure analysis in the quiet corona has yielded consistent results (e.g., Feldman et al. 1999a; Warren & Warshall 2002). The isothermal DEM calculation for the Si lines is illustrated in Figure 2, where the best-fit parameters are shown. Here, we also display the emission measure loci curves defined by

$$\mathrm{EM}(T) \equiv \frac{4\pi I_\lambda}{\epsilon_\lambda(n_e, T)}. \quad (4)$$

Previous analysis in the quiet corona above the limb has shown that these curves tend to intersect at a point, suggesting isothermal plasma. As noted before, we solve for the best-fit parameters through χ^2 minimization rather than estimating them by eye as has been done previously (e.g., Feldman et al. 1998).

The best-fit temperature is similar to the values of $\log T_0 = 6.05$ determined by Landi et al. (2002) and $\log T_0 = 6.01$ determined by Allen et al. (2000). Other studies yield somewhat higher temperatures of $\log T_0 \sim 6.15$ (e.g., Raymond et al. 1997; Feldman et al. 1999a; Warren 1999; Warren & Warshall 2002). Additionally, as indicated by the values listed in Table 3, the computed intensities of the Si VII and Si X lines are consistent with each other to within about ±15%. This calculation depends

Table 2
Si, S, and O Intensities Measured in the Quiet Corona above the Limb with EIS

Ion	λ	T_{max}	Transition	L1	L2	ϵ_λ	I_{obs}	σ_{Iobs}	
O VI	183.937	5.47	$1s^2\ 2p\ ^2P_{1/2}$–$1s^2\ 3s\ ^2S_{1/2}$	2	4	4.66e-25	2.81 ±	0.05	?
O VI	184.117	5.47	$1s^2\ 2p\ ^2P_{3/2}$–$1s^2\ 3s\ ^2S_{1/2}$	3	4	9.36e-25	4.82 ±	0.10	?
Si VII	275.352	5.77	$2s^2\ 2p^4\ ^3P_2$–$2s\ 2p^5\ ^3P_2$	1	6	4.55e-24	11.54 ±	0.07	♡
Si VII	275.665	5.77	$2s^2\ 2p^4\ ^3P_1$–$2s\ 2p^5\ ^3P_1$	2	7	7.04e-25	1.81 ±	0.05	♡
Si VII	278.445	5.77	$2s^2\ 2p^4\ ^3P_1$–$2s\ 2p^5\ ^3P_2$	2	6	1.45e-24	2.95 ±	0.19	♡
Si IX	258.073	6.05	$2s^2\ 2p^2\ ^1D_2$–$2s\ 2p^3\ ^1D_2$	4	13	1.31e-25	5.08 ±	0.08	♡
Si X	253.791	6.13	$2s^2\ 2p\ ^2P_{1/2}$–$2s\ 2p^2\ ^2P_{3/2}$	1	10	4.21e-25	12.84 ±	0.13	♡
Si X	258.375	6.13	$2s^2\ 2p\ ^2P_{3/2}$–$2s\ 2p^2\ ^2P_{3/2}$	2	10	2.19e-24	71.30 ±	0.18	♡
Si X	261.058	6.13	$2s^2\ 2p\ ^2P_{3/2}$–$2s\ 2p^2\ ^2P_{1/2}$	2	9	1.30e-24	43.34 ±	0.13	♡
Si X	271.990	6.13	$2s^2\ 2p\ ^2P_{1/2}$–$2s\ 2p^2\ ^2S_{1/2}$	1	8	9.76e-25	37.62 ±	0.10	♡
Si X	277.255	6.13	$2s^2\ 2p\ ^2P_{3/2}$–$2s\ 2p^2\ ^2S_{1/2}$	2	8	7.99e-25	28.83 ±	0.11	♡
S X	264.233	6.15	$2s^2\ 2p^3\ ^4S_{3/2}$–$2s\ 2p^4\ ^4P_{5/2}$	1	6	8.21e-25	34.77 ±	0.11	?

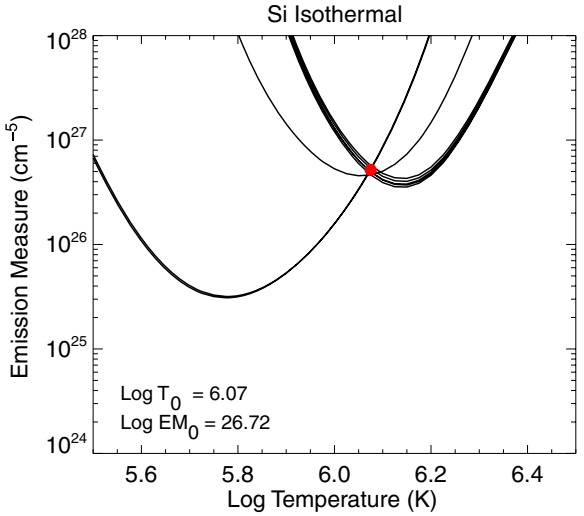

Figure 2. Emission measure analysis of the Si emission lines observed with EIS. In these calculations the density is held constant at $\log n_e = 8.35$.
(A color version of this figure is available in the online journal.)

Table 3
Isothermal Model Applied to the Si Lines

Ion	Wavelength	I_{calc}	I_{obs}	I_{calc}/I_{obs}
Si VII	275.352	11.41	11.54	0.99
Si VII	275.665	1.83	1.81	1.01
Si IX	258.073	5.71	5.08	1.12
Si X	253.791	14.32	12.84	1.12
Si X	258.375	74.43	71.30	1.04
Si X	261.058	45.39	43.34	1.05
Si X	271.990	34.09	37.62	0.91
Si X	277.255	27.89	28.83	0.97

on the density, which we have assumed to be $\log n_e = 8.35$ in this calculation. If we allow the density to be a free parameter in the minimization then we find $\log n_e = 8.22$. These values are within the range of possible densities. We will discuss the densities derived from the various line ratios and DEM inversion methods in detail at the end of this section.

The generally good agreement among the observed Si lines is not matched by the observed Fe spectrum. Emission measure loci plots for all of the Fe lines, which are shown in Figure 3, do not reveal any discernible pattern and do not suggest either isothermal or multithermal plasma.

If the atomic data, the assumed density, and the observed intensities were mutually consistent then all of the emission measure loci curves for a given ion would lie very close together, as they do for Si VII and Si X. Closer inspection of the emission measure loci curves for Fe shown in Figure 3 suggests that for each ion there are several emission lines that are mutually consistent and others that are discrepant by varying amounts. Here, we identify these lines and discuss previously identified blends.

Fe VIII. The emission measure loci for 185.213 and 186.601 Å lines are consistent, but the curve for 194.663 Å is about a factor of 2 higher. Brown et al. (2008) indicate a possible blend of Fe VIII 194.663 Å with O V 195.593 Å, which would have negligible intensity at this height above the limb. In the core of an active region Fe VIII 185.213 Å is blended with Ni XVI 185.251 Å and Fe VIII 186.601 Å is blended with Ca XIV 186.610 Å. As stated earlier, the ionization fraction for Fe VIII may need revision, so these lines should be used with caution.

Fe IX. The newly identified 188.497, 189.941, and 197.862 Å lines are all in good agreement. The emission measure loci for Fe IX 171.073 Å is off by about a factor of 2. The effective area for EIS at this wavelength is very low, making the observed intensity highly uncertain.

Fe X. The 174.532, 177.239, and 184.536 Å lines are all in agreement. The Fe X 190.038, 207.449, and 257.262 lines are not. The 184.536 and 190.038 Å lines originate in the same upper level and form a branching ratio. The theoretical ratio, however, is 3.56 while the observed ratio is 2.70. The Fe X 257.262 line forms a density sensitive ratio with 184.536 and 190.038 Å, but the problems with the emission measure loci suggests that the densities derived from this ratio are not consistent with the densities derived from the Si ratio. Brown et al. (2008) indicate a possible blend of Fe X 184.536 Å with Ar XI 184.524 Å, which would be a problem for active region observations.

Fe XI. The 180.401, 182.167, 188.216, and 192.813 Å lines are all in agreement. The emission measure loci for 188.299, 257.547, and 257.772 Å differ by factors of 2–4. The 182.167 and 188.216 Å lines form a density sensitive line ratio. Brown et al. (2008) indicate that Fe XI 180.401 Å is blended with Fe X 180.407 Å. Using the isothermal emission measure determined from Si to estimate the intensities of the two lines suggests that the Fe X contribution to the observed intensity is about 10%. There are O V lines that can make important contributions to the observed Fe XI 192.813 Å line profile during transient events (Ko et al. 2009).

Fe XII. The Fe XII 186.880, 192.394, 193.509, 195.119, and 196.640 Å lines are all in relatively good agreement. The

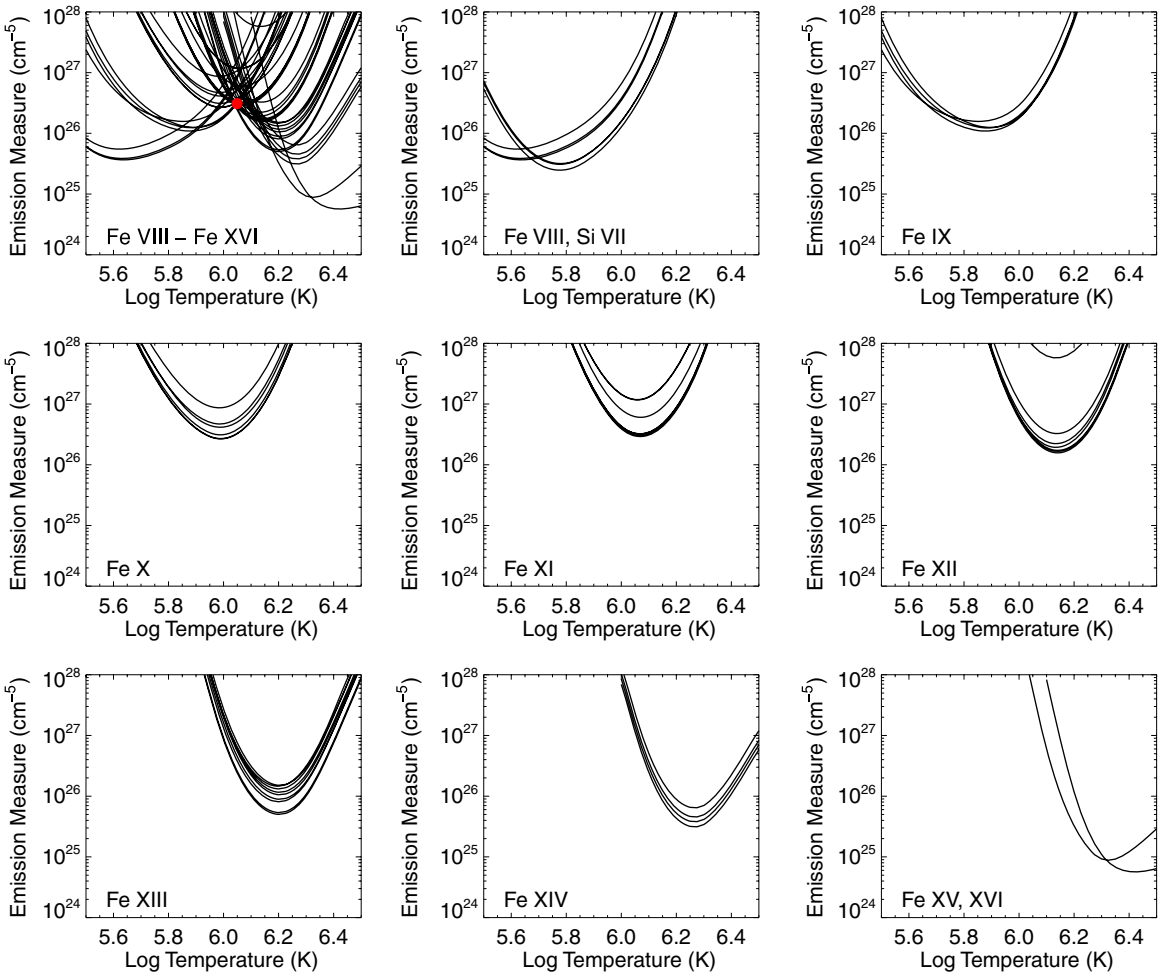

Figure 3. Emission measure loci plots for Fe VIII–XVI emission lines observed with EIS. These plots illustrate the problems with a number of the emission lines observed within this wavelength range. The red dot is the isothermal emission measure derived from the Si lines. In these calculations the density is held constant at $\log n_e = 8.35$.

(A color version of this figure is available in the online journal.)

203.720 and 256.925 Å lines differ by factors of 2 and 30, respectively. The 186.880 and 196.640 Å lines form density sensitive ratios when paired with any of the 192.394, 193.509, and 195.119 Å lines. There is a S XI line at 186.84 Å, but it is generally weak compared with the Fe XII 186.880 line (Young et al. 2009). In active regions, Young et al. (2009) note that there is an Fe XII 195.18 Å line that becomes important at high densities. This component is generally small but can impact Doppler shift and line width measurements with the Fe XII 195.119 Å line.

Fe XIII. The 196.525, 197.434, 200.021, 202.044, and 203.826 Å lines are generally consistent. The emission measure loci for 201.121, 204.937, 246.208, and 251.953 are all offset by varying amounts. The 196.525 and 203.826 Å lines form density sensitive ratios with 202.044 Å. There is a possible blend of Fe XIII 196.525 Å with Fe VIII 196.65 Å, but the Fe VIII line is believed to be weak (Young et al. 2009). Brown et al. (2008) indicate that Fe XIII 201.121 Å is blended with Fe XII 201.121 Å.

Fe XIV. The 211.316, 270.519, and 274.203 Å emission measure loci curves are all relatively close to each other while the curve for 264.787 Å is offset. The 264.787 and 274.203 Å lines form a density sensitive pair, but this ratio should be in the low density limit in the quiet Sun. There is a blend of Fe XIV 274.203 Å with Si VII 274.175 Å. Young et al. (2007) indicate that the Si VII 274.175 Å intensity is less than 0.25 times the intensity of Si VII 275.352 Å. The ratio of the Si lines is sensitive to density, however, and for the low densities measured above the limb the ratio is calculated to be about 10%, suggesting a negligible contribution of Si VII to the Fe XIV 274.203 Å intensity measured here.

Fe XV and *Fe XVI.* There is only a single Fe XV emission line in the EIS wavelength ranges. There are several Fe XVI lines present, but as indicated earlier, no emission is observed in any of these lines. The intensity given in Table 1 for Fe XVI 262.984 Å serves only as an upper bound and limits the peak temperature in the emission measure. There is no independent verification of the consistency of these lines.

We have used the lines identified here by their internal consistency to compute the emission measure using the three different models. Both the emission measures and the emission measure loci are shown in Figure 4. The isothermal solution for these selected Fe lines is very similar the solution found for the Si lines. The best-fit temperature is $\log T = 6.05$, compared with 6.07 for the Si lines. It is clear, however, that the isothermal model cannot reproduce both the low temperature emission (Fe IX–XIII) and the emission observed in the higher temperature lines (Fe XIV–XVI). The intensities for the high temperature

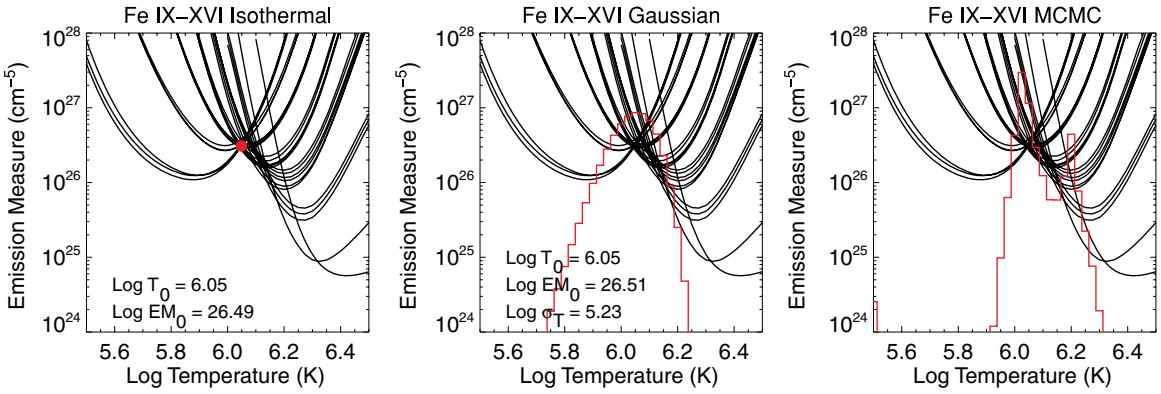

Figure 4. Differential emission measures derived from Fe IX–XVI and different emission measure models (isothermal, Gaussian, and MCMC). For the Gaussian and MCMC models the temperature times the differential emission measure is displayed. The MCMC DEM has the lowest χ^2 and best reproduces the observed intensities. In these calculations the density is held constant at $\log n_e = 8.35$.

(A color version of this figure is available in the online journal.)

lines computed from the isothermal emission measure are systematically too small by a factor of about 4.

This systematic discrepancy suggests that the plasma in the quiet corona is not isothermal. To investigate this we have applied the Gaussian DEM algorithm to the Fe lines. If we include only the Fe IX–XIII lines we obtain a very narrow emission measure distribution ($\sigma_T = 4.8$). Including the Fe XIV–XVI lines leads to a somewhat broader emission measure distribution ($\sigma_T = 5.2$), but only a marginal improvement between the observed and calculated intensities. For this case the observed intensities are systematically larger than what is calculated from the Gaussian emission measure by about a factor of 2.

The failure of the Gaussian emission measure model to reproduce all of the observed line emission is due in large part to the symmetry that this model imposes on the DEM. Increases in the emission measure at higher temperature must be accompanied by increases at lower temperatures, and this would lead to discrepancies in the Fe IX and Fe X intensities. The MCMC algorithm does not assume any functional form for the emission measure and provides for more flexibility. The differential emission measure calculated using the MCMC algorithm is displayed in Figure 4 and calculated intensities are given in Table 4. In this case, the agreement between the observed and calculated intensities is improved for the high temperature lines while maintaining the good agreement at the lower temperatures. This is achieved by the introduction of a high-temperature tail in the differential emission measure in addition to the strong peak near 1 MK. The strong peak in the emission measure is consistent with previous work. Previous studies have usually employed relatively restrictive parameterizations for the emission measure and would not have been able to identify this high-temperature component.

The best-fit parameters for the Si and Fe isothermal emission measure calculations show a significant discrepancy in the magnitude of the emission measure, with the Si emission measure being about 60% larger ($\log \mathrm{EM}_0 = 26.49$ for Fe and 26.72 for Si). We find a similar difference if we use the MCMC DEM to infer the intensities of the Si lines. Curiously, the Si lines all fall on the long wavelength detector while the Fe lines all fall on the short wavelength detector. None of the long wavelength Fe X, XI, XII, or XIII lines are consistent with the short wavelength lines from the same ion. Similarly, the high-temperature lines, whose intensities the isothermal models systematically underpredict, generally lie on the long wavelength detector. This suggests that calibration differences between the two detectors might explain at least part of these discrepancies. While this explanation may sound plausible it does not withstand closer scrutiny. Perhaps most importantly, the magnitude of the discrepancy between the calculated and observed Fe XIV–XVI intensities is much larger than the difference between the Si and Fe isothermal emission measures. If the observed values were reduced by a factor of 1.6 the calculated intensities would still be off by a factor of 3 or more. One Fe XIV line does appear on the short wavelength detector (211.316 Å) and its behavior is similar to the long wavelength Fe XIV lines. Finally, the discrepancies in the emission measure loci curves discussed previously do not show any systematic variation with wavelength. With these data

Table 4
MCMC Model Applied to the Fe IX–XVI Lines

Ion	Wavelength	I_{calc}	I_{obs}	$I_{\mathrm{calc}}/I_{\mathrm{obs}}$
Fe IX	188.497	34.13	31.28	1.09
Fe IX	189.941	18.02	15.36	1.17
Fe IX	197.862	24.50	21.02	1.17
Fe X	174.532	560.17	572.57	0.98
Fe X	177.239	304.81	308.28	0.99
Fe X	184.536	119.94	142.17	0.84
Fe XI	180.401	415.93	432.24	0.96
Fe XI	182.167	53.84	58.50	0.92
Fe XI	188.216	196.01	224.90	0.87
Fe XI	192.813	50.16	57.73	0.87
Fe XII	186.880	33.11	35.17	0.94
Fe XII	192.394	88.03	79.48	1.11
Fe XII	193.509	185.60	177.53	1.05
Fe XII	195.119	277.87	274.67	1.01
Fe XII	196.640	9.04	11.03	0.82
Fe XIII	196.525	1.71	2.71	0.63
Fe XIII	197.434	5.24	7.10	0.74
Fe XIII	200.021	6.37	9.43	0.68
Fe XIII	202.044	126.16	157.66	0.80
Fe XIII	203.826	27.46	25.02	1.10
Fe XIII	204.937	7.88	8.19	0.96
Fe XIV	211.316	30.71	39.47	0.78
Fe XIV	270.519	7.97	6.96	1.14
Fe XIV	274.203	17.19	18.31	0.94
Fe XV	284.160	28.72	21.20	1.35
Fe XVI	262.984	0.17	0.42	0.42

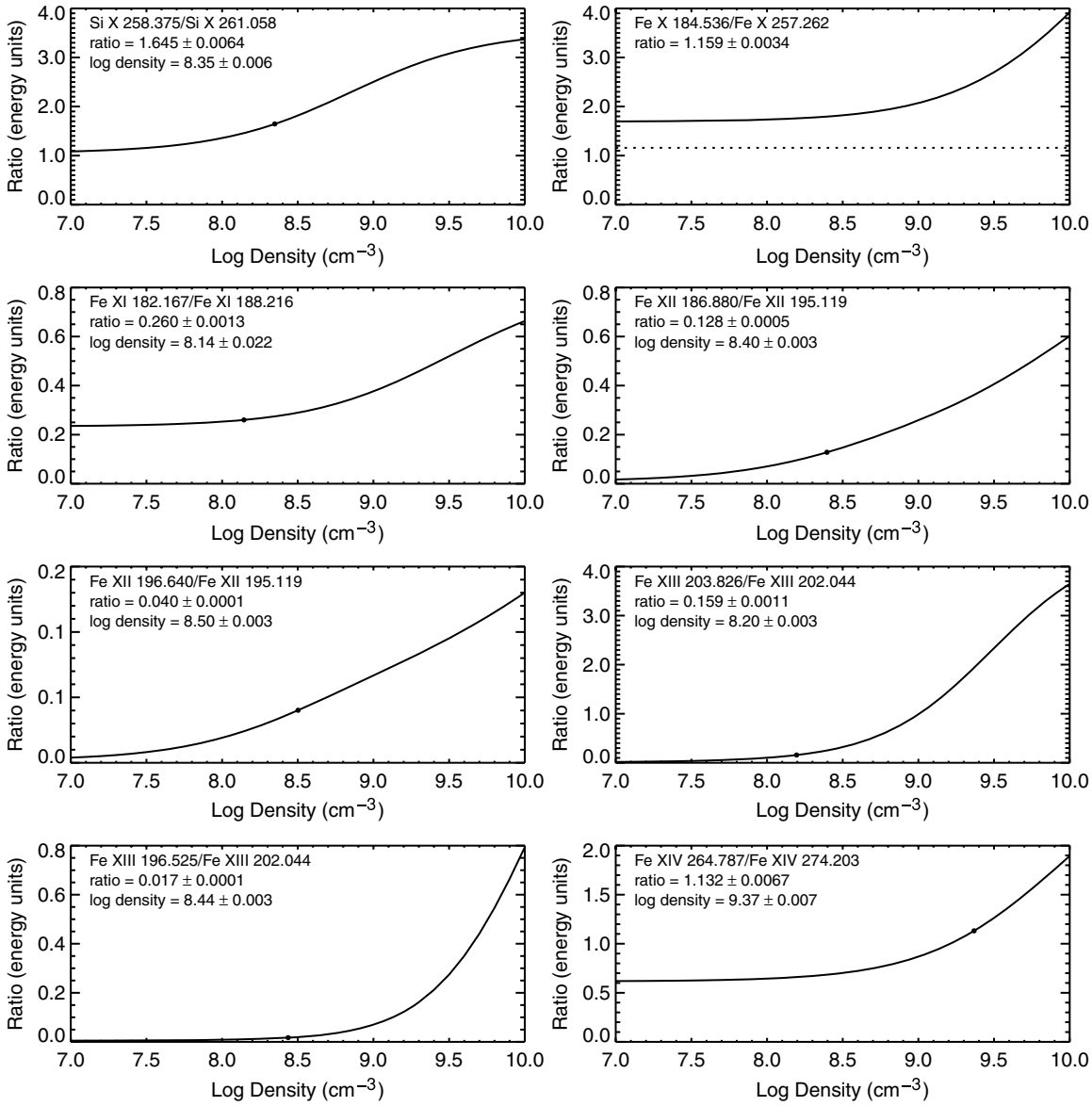

Figure 5. Electron densities derived from eight density-sensitive line ratios. The emissivities were evaluated at $\log T = 6.05$.

we find no evidence that there is a problem with the relative calibration of the detectors.

When computing the line intensity the density and temperature both play an important role in determining the emissivity. This makes it difficult to determine the temperature and density independently. One way of addressing this issue is to allow both parameters to vary while using Equation (1) to find the optimal parameters. We have done this in applying the isothermal model to the Si and Fe IX–XIII lines and we generally find somewhat different densities. The EIS wavelength ranges contain a large number of density sensitive line ratios (see Young et al. 2007 for a summary) and we can use these data to compare the results. In Figure 5, we show the densities derived directly from Si X 258.375/261.058 Å, Fe X 184.536/257.262 Å, Fe XI 182.167/188.216 Å, Fe XII 186.880/195.119 Å, Fe XII 196.640/195.119 Å, Fe XIII 196.525/202.044 Å, Fe XIII 203.826/202.044 Å, and Fe XIV 264.787/274.203 Å. The emissivities are computed assuming $\log T = 6.05$, as derived from the isothermal emission measure analysis.

These ratios show some significant differences. The Fe X and Fe XIV ratios give useless results, with the Fe X being below the low density limit and Fe XIV yielding a density an order of magnitude larger than the others. The other ratios yield values ranging from $\log n_e = 8.14$ to 8.50. These values are generally consistent with the densities determined in earlier analysis of quiet Sun limb observations, e.g., $\log n_e \sim 8.3$ by Doschek et al. (1997) and $\log n_e \sim 8.5$ by Landi et al. (2002). Based on previous analysis, the Si X ratio is probably the most reliable ratio of this group. We note that the densities from the Fe lines are scattered around the density derived from Si and if we average the Fe densities together we obtain 8.34 ± 0.16. This is a variation of about a factor of 2. To simplify the discussion, all of the plots and tables assume a density of $\log n_e = 8.35$.

The large region that we have used for computing an average spectrum leads to very small statistical errors for the measured intensities. Lang et al. (2006) calculate the uncertainty in the absolute radiometric calibration for EIS to be 22%. This additional uncertainty can be easily added in quadrature to the values given in Tables 1 and 2. We have rerun all of the DEM calculations including the calibration uncertainties and obtained very similar results. The biggest differences are for the MCMC algorithm, which yields a somewhat smoother emission measure

at high temperatures. Variations in the detailed structure of the emission measure are not surprising given the ill-posed nature of the emission measure inversion problem (e.g., Craig & Brown 1976).

4. ABUNDANCES

To accurately compute the magnitude of the radiative losses in the corona we must have some measure of the coronal composition. Understanding radiative cooling is important for modeling the evolution of coronal loops (e.g., Warren et al. 2003; Winebarger & Warren 2004). Spatially averaged measurements suggest that the low FIP elements, such as Fe, Si, and Mg, are all enriched in the corona relative to high FIP elements, such as C, N, and O by about a factor of 4 (e.g., Feldman et al. 1998). Temporally resolved measurements in active regions indicate, however, that this enhancement may change with time (Widing & Feldman 2001), with newly emerged active regions having more photospheric abundances (i.e., no enrichment of the low FIP elements). This suggests the need for more systematic abundance measurements.

Several abundance diagnostics in the EIS wavelength ranges have been discussed by Feldman et al. (2009). For coronal plasma the most useful EIS emission lines from high FIP elements are S x 264.233 Å and S xiii 256.686 Å. In these quiet Sun data only the S x 264.233 Å line appears. The FIP for S is 10.3 eV and it lies at the boundary between the high and low FIP elements. Some measurements (e.g., Feldman et al. 1998) show a partial enrichment of S in the corona. Other measurements (e.g., Feldman et al. 1992) indicate essentially photospheric abundances. The general trend is for S to behave somewhat differently than the low FIP elements, and S x can be used as a proxy for measuring relative abundance variations in EIS observations of the corona. For these observations above the quiet corona it is also possible to use O vi as a high FIP line (e.g., Feldman et al. 1998). O vi is Li-like and the ionization fraction extends to high temperatures.

In calculating the emissivities we have assumed a coronal composition with $A_{\rm Fe} = 8.10$, $A_{\rm Si} = 8.10$, $A_{\rm O} = 8.89$, and $A_{\rm S} = 7.27$ (Feldman et al. 1992). The photospheric composition of Grevesse & Sauval (1998) has $A_{\rm Fe} = 7.50$, $A_{\rm Si} = 7.55$, $A_{\rm O} = 8.83$, and $A_{\rm S} = 7.33$. If we use the MCMC emission measure computed from the Fe lines to compute the intensities of O vi 183.937, 184.117, and S x 264.233 Å we obtain values of 0.8, 1.6, and 15.0 erg cm^{-2} s^{-1} sr^{-1}, respectively. The observed intensities in this region are 2.8, 4.8, and 34.8 erg cm^{-2} s^{-1} sr^{-1}, suggesting that the relative abundances of the Feldman et al. (1992) are not consistent with these data. The abundance of S and O in the corona would need to be increased by about a factor of 2.9 or the abundance of Fe decreased by about a factor of 2.9 to resolve this discrepancy. Similarly, the difference in the emission measures derived from the Si and Fe lines could be resolved by adjusting their relative abundances.

5. QUIET SUN DISK

The observations taken above the limb provide an opportunity to study a high signal to noise spectrum derived from an average over a largely homogeneous region. This analysis has revealed many problems with interpreting the observed intensities. These problems could be due to blends with other lines, errors in the calibration, or blends with other lines. Since the morphology of the quiet solar atmosphere changes with temperature (e.g., Feldman et al. 1999b) examining spatially resolved images in these emission lines offers a means of identifying previously unidentified blends in the lines.

Most EIS observations preserve the information from only a few narrow spectral windows. Observations that contain the full wavelength range are typically small in size. We have found several observations that contain the full wavelength range and cover a relatively large region on the Sun (up to $128'' \times 512''$). For one of these observations (taken on 2007 November 15 11:14 UT) we have processed the data and constructed rasters in as many of the emission lines given in Tables 1 and 2 as possible. These rasters are computed by performing Gaussian fits to the spectral lines at each spatial position. Unfortunately, some emission lines from the limb spectra are too weak to fit in the spatially resolved disk spectra.

The rasters for many of the emission lines of interest are shown in Figures 6 and 7. These rasters suggest a progression from small-scale structures that correspond to the magnetic network at low temperatures to much longer loops, with no network pattern at high temperatures. Surprisingly, there is little evidence for blending in many of the problem emission lines. For example, the Fe x 184.536 and 190.038 Å rasters are nearly identical. The contrast in the Fe x 257.262 Å raster is somewhat different than in the other rasters, but this line is sensitive to density and this is to be expected. Similarly, the Fe xi 188.216 and 188.299 Å rasters are nearly identical. There is some evidence for small bright features in the Fe xi 192.813 Å raster, suggestive of O v emission. For Fe xii the discrepant 203.720 Å rasters appears to be consistent with the rasters from the other lines. The Fe xii 256.925 Å line does appear to be blended with a cooler line. The contrast between the center of this raster and the structures in the north and south is smaller than for the other Fe xii lines. For similar reasons, the Fe xiv 264.787 Å also appears to be blended with a cooler line.

6. DISCUSSION

We have presented a detailed analysis of spectroscopic observations taken in the quiet corona above the limb with the EIS instrument on *Hinode*. The strongly peaked differential emission measure calculated from the Si and Fe lines are generally consistent with each other and with previous measurements. This suggests that despite the complexity of the Fe atom, accurate differential emission measure calculations are possible with the strongest emission lines observed with EIS. Our analysis validates some of the initial EIS emission measure calculations for coronal loops (e.g., Warren et al. 2008; Tripathi et al. 2009), which emphasize the lines given in Table 4.

Using the MCMC DEM algorithm we find evidence for a tail in the emission measure that extends to high temperatures. Such features are extremely important to theories of coronal heating based on the impulsive release of energy (e.g., Cargill & Klimchuk 2004; Patsourakos & Klimchuk 2006, 2008). It will be interesting to see if similar features of the DEM are observed in active region loops.

The densities measured from six of the eight density sensitive line ratios that we considered are generally consistent with each other and with previous measurements. There is, however, considerable scatter in the measured densities. Measurements in active regions suggest that these differences are systematic, with the Fe xii 186.880/195.119 Å density being systematically higher than the Fe xiii 203.826/202.044 Å density (Young et al. 2007).

This work has highlighted problems with the analysis of many emission lines in the EIS spectral wavelengths. These

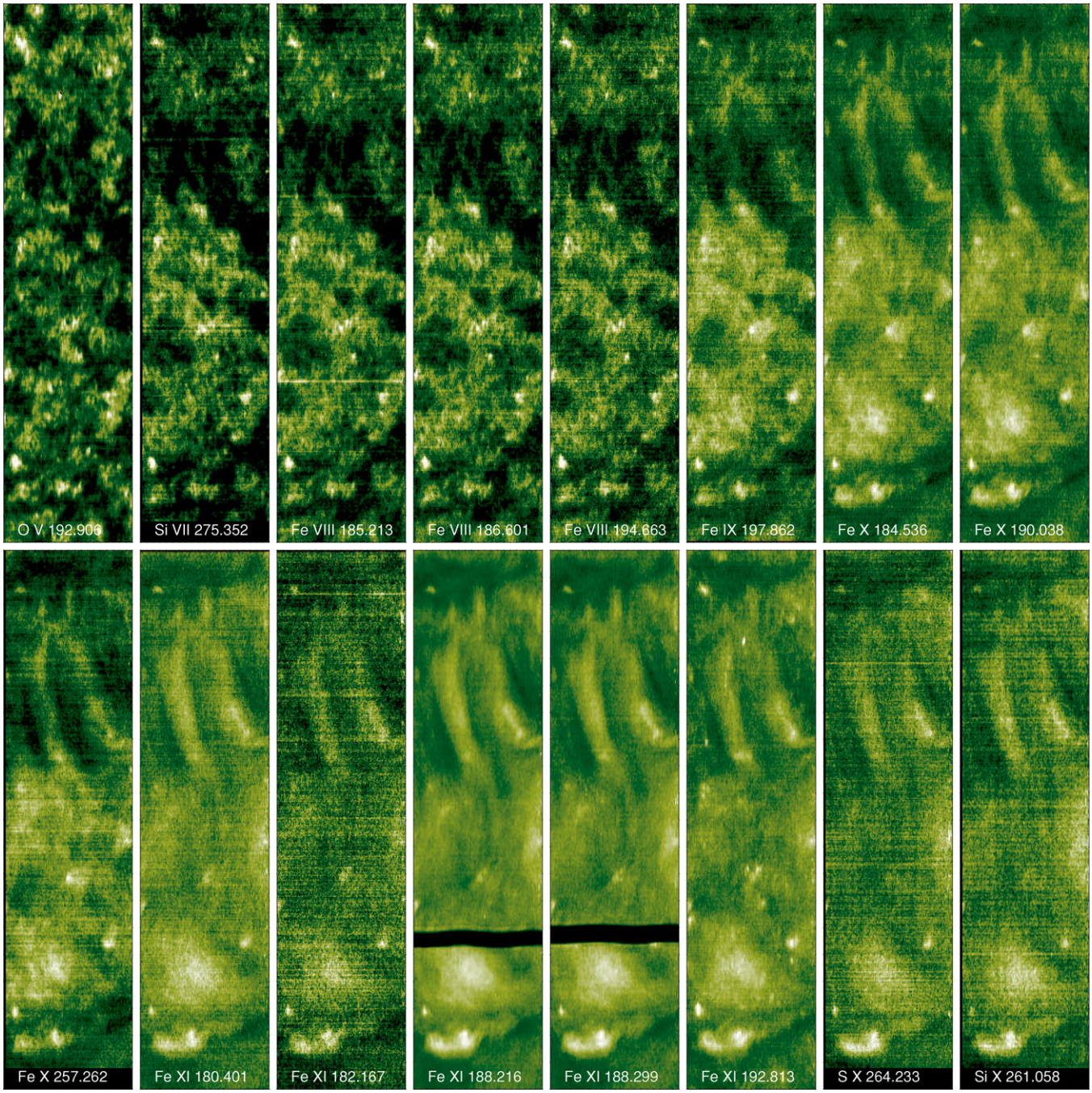

Figure 6. EIS rasters from observations of the quiet solar disk taken on 2007 November 15 from 11:13:59 to 14:12:17 UT. The 1″ slit has been stepped over a region 128″ × 512″ in size, and an 80 s exposure has been taken at each slit position. Rasters for O v–Si x are shown. These spatially resolved disk measurements allow for the morphology of different emission lines from the same ion to be compared. The Fe xi 192.813 Å shows a small contribution from O v.

(A color version of this figure is available in the online journal.)

differences result from some combination of errors in the atomic data, blends with unidentified lines, and uncertainties with the EIS calibration. Some of these difficulties are clearly due to the errors in the atomic data or assumptions that have been made in using them. The observations suggest that the ionization fractions for Fe viii, for example, may need to be shifted to high temperatures. The quiet Sun disk rasters for Fe x 190.038 Å and 257.262 Å, Fe xi 188.299 Å, Fe xii 203.720 Å, and Fe xiii 251.953 Å do not appear to be blended with other lines. These rasters do suggest blends for Fe xii 256.925 Å and Fe xiv 264.787 Å. The possibility of errors in the EIS relative calibration is unclear. The Fe xiv 211.316 Å line is consistent with Fe xiv 270.519 and 274.203 Å, suggesting that there are no significant discrepancies. It is unsettling, however, that none of the Fe x, xi, xii, and xiii lines near 250 Å agree with the lines at shorter wavelengths.

The use of EIS observations for abundance measurements is still unsettled. The ratios of the S and O lines to Si and Fe do not yield results that are consistent with existing sets of solar abundances. It is unclear how these issues can be resolved at present. Despite this difficulty it is still possible to use EIS observations to investigate spatial and temporal variations in the

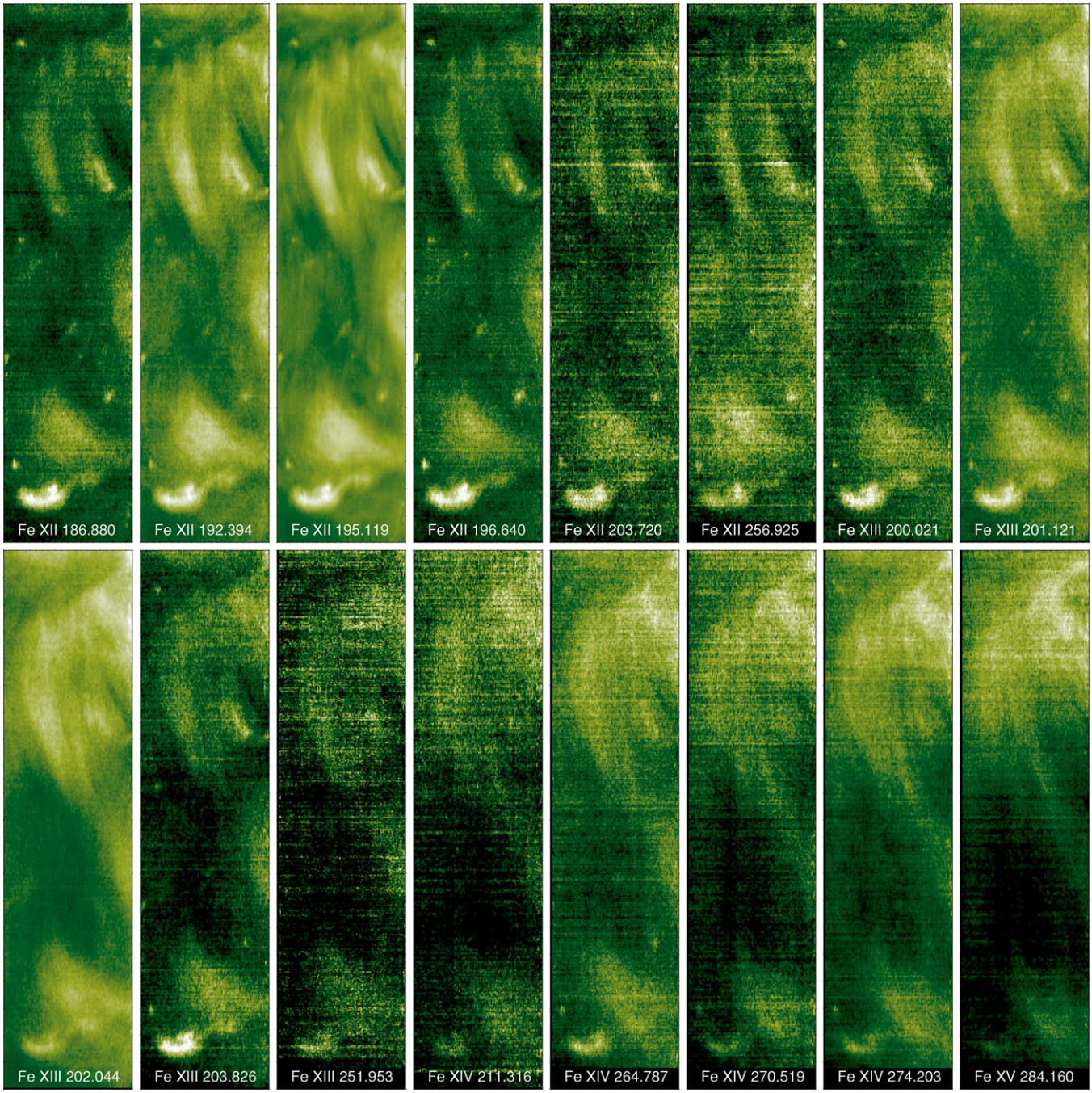

Figure 7. Same region as is shown in Figure 6 except that Fe XII–Fe XV are shown. The Fe XII 256.925 Å and Fe XIV 264.787 Å lines appear to have excess emission in the center of the rasters, suggesting blends with cooler emission lines.

(A color version of this figure is available in the online journal.)

solar composition. This is illustrated in Figure 6, where we can see spatially resolved images in S X and Si X. When combined with emission measure analysis, observations such as these can be used to understand the how much the composition varies from structure to structure in the solar corona. Work on the analysis of quiet Sun disk spectra are currently in progress and will be reported in a future paper Brooks et al. (2009).

Hinode is a Japanese mission developed and launched by ISAS/JAXA, with NAOJ as domestic partner and NASA and STFC (UK) as international partners. It is operated by these agencies in cooperation with ESA and NSC (Norway).

REFERENCES

Allen, R., Landi, E., Landini, M., & Bromage, G. E. 2000, A&A, 358, 332
Brooks, D. H., Warren, H. P., Williams, D. R., & Watanabe, T. 2009, ApJ, submitted
Brown, C. M., Feldman, U., Seely, J. F., & Korendyke, C. M. 2008, ApJS, 176, 511
Cargill, P. J., & Klimchuk, J. A. 2004, ApJ, 605, 911
Craig, I. J. D., & Brown, J. C. 1976, A&A, 49, 239
Culhane, J. L., et al. 2007, Sol. Phys., 243, 19
Delaboudinière, J.-P., et al. 1995, Sol. Phys., 162, 291
Doschek, G. A., Warren, H. P., Laming, J. M., Wilhelm, K., Lemaire, P., Schühle, U., & Moran, T. G. 1997, ApJ, 482, L109
Feldman, U., Doschek, G. A., Schühle, U., & Wilhelm, K. 1999a, ApJ, 518, 500

Feldman, U., Mandelbaum, P., Seely, J. F., Doschek, G. A., & Gursky, H. 1992, ApJS, 81, 387
Feldman, U., Schühle, U., Widing, K. G., & Laming, J. M. 1998, ApJ, 505, 999
Feldman, U., Warren, H. P., Brown, C. M., & Doschek, G. A. 2009, ApJ, 695, 36
Feldman, U., Widing, K. G., & Warren, H. P. 1999b, ApJ, 522, 1133
Grevesse, N., & Sauval, A. J. 1998, Space Sci. Rev., 85, 161
Kashyap, V., & Drake, J. J. 1998, ApJ, 503, 450
Kashyap, V., & Drake, J. J. 2000, Bull. Astron. Soc. India, 28, 475
Ko, Y.-K., Doschek, G. A., Warren, H. P., & Young, P. R. 2009, ApJ, 697, 1956
Korendyke, C. M., et al. 2006, Appl. Opt., 45, 8674
Landi, E., Del Zanna, G., Young, P. R., Dere, K. P., Mason, H. E., & Landini, M. 2006, ApJS, 162, 261
Landi, E., Feldman, U., & Dere, K. P. 2002, ApJ, 574, 495
Lang, J., et al. 2006, Appl. Opt., 45, 8689
Mazzotta, P., Mazzitelli, G., Colafrancesco, S., & Vittorio, N. 1998, A&AS, 133, 403
Parker, E. N. 1972, ApJ, 174, 499
Parker, E. N. 1983, ApJ, 264, 642
Patsourakos, S., & Klimchuk, J. A. 2006, ApJ, 647, 1452
Patsourakos, S., & Klimchuk, J. A. 2008, ApJ, 689, 1406
Raymond, J. C., et al. 1997, Sol. Phys., 175, 645
Tripathi, D., Mason, H. E., Dwivedi, B. N., Del Zanna, G., & Young, P. R. 2009, ApJ, 694, 1256
Warren, H. P. 1999, Sol. Phys., 190, 363
Warren, H. P., Ugarte-Urra, I., Doschek, G. A., Brooks, D. H., & Williams, D. R. 2008, ApJ, 686, L131
Warren, H. P., & Warshall, A. D. 2002, ApJ, 571, 999
Warren, H. P., Winebarger, A. R., & Mariska, J. T. 2003, ApJ, 593, 1174
Widing, K. G., & Feldman, U. 2001, ApJ, 555, 426
Winebarger, A. R., & Warren, H. P. 2004, ApJ, 610, L129
Young, P. R. 2009, ApJ, 691, L77
Young, P. R., Del Zanna, G., Mason, H. E., & Dere, K. P. 2007, PASJ, 59, 857
Young, P. R., Watanabe, T., Hara, H., & Mariska, J. T. 2009, A&A, 495, 587